ISSN 2176-5480

22nd International Congress of Mechanical Engineering (COBEM 2013)
November 3-7, 2013, Ribeirão Preto, SP, Brazil

COMPARISON BETWEEN ULTRASONIC SYNTHETIC APERTURE IMAGING METHODS USING THE PHASE OF SIGNALS FOR PLATE-LIKE STRUCTURES

Vander Teixeira Prado
Ricardo Tokio Higuti
Cláudio Kitano
Faculdade de Engenharia de Ilha Solteira, UNESP - Universidade Estadual Paulista, Department of Electrical Engineering, Av. Brasil, 56 (centro), CEP 15385-000 – Ilha Solteira, SP, Brasil
vandertprado@gmail.com, tokio@dee.feis.unesp.br, kitano@dee.feis.unesp.br

Abstract. *Ultrasonic synthetic aperture techniques reduce the complexity and the cost of imaging systems, compared to phased arrays, demanding less multiplexed emitter/receiver channels. The main lobe width, the side lobe levels and the existence of grating lobes (in sparse arrays), are also directly related to the quality of images. Conventional imaging methods employ only the amplitude of the signals in the beamforming process, not considering the phase information. Three techniques using the phase information are compared to the conventional amplitude descriptor: the Sign Coherence Factor (SCF), which uses the phase diversity at the aperture data; the Coherence Factor Map (CFM), that presents a spectral analysis of the phase dispersion; and the analysis of the instantaneous phase (IP) image, which applies a threshold based on a statistical analysis of noise and the number of elements. The techniques are applied to full-populated and sparse arrays in non-destructive testing using Lamb waves. The use of phase information is better than only the amplitude for all cases, reducing dead zone and improving contrast. The SCF images have better resolution, contrast and less image artifacts than CFM images, which in turn present defects with higher intensities, which can be an advantage in threshold usage for defect indication. IP images obtains better defect representations for farther defects once it uses only the phase information, and the attenuation effect due to propagation losses is less significant.*

Keywords: *phase, ultrasonic images, arrays, synthetic aperture, plate-like structures*

1. INTRODUCTION

Ultrasound has been increasingly used in non-destructive testing techniques owing to advantages like ease and speed of test, high sensitivity, it does not produce changes in the inspected materials and it propagates in different types of media (solid, liquid, gaseous). Longitudinal or shear bulk waves, as well as guided waves, can be used for damage detection or material characterization.

When one of the dimensions of the structure is smaller than the others, such in thin plates, Lamb waves can be coupled. They propagate over long distances, due to low attenuation, inspecting relatively large areas without the necessity of moving the transducers. They can be used to make inspection of the whole transversal section of the plate, being sensitive to different types of defects, such as through holes, corrosion, thickness variation and surface defects (Rose, 2000; Alleyne and Cawley, 1992; Su *et al.*, 2006).

An image of the plate can be obtained by the use of arrays. An ultrasonic array is a set of transducers geometrically organized to control the acoustic beam electronically (Drinkwater and Wilcox, 2006). The quality of the image depends on various parameters: array configuration, number of elements, transducer geometry (Diamanti *et al.*, 2007; Yu and Giurgiutiu, 2007; Michaels, 2008), beamforming technique, propagation wave, signal-to-noise ratio and radiation pattern characteristics as main lobe width, side lobe levels and grating lobes.

When all array elements, or part of them, are excited simultaneously, known as phased array, a transmit/receive channel dedicated to each element is needed, which reduces the time of data acquisition and process significantly. On the other hand it increases the complexity and the cost of the system. In synthetic aperture (SA) techniques one element is used in emission and at least one element is used in reception for each transmitter (Ylitalo and Ermert, 1994). The data is post-processed and signals are delayed-and-summed (DAS method – delay-and-sum) to dynamically focus the region of interest of the structure. In SA techniques the hardware complexity is reduced, without the necessity of reducing the number of elements of the aperture. As in general the dynamics of the structure is relatively slow, this type of signal acquisition and post-processing is adequate, as it is not necessary to have too many images per second.

By considering a linear array of N elements and pitch d, illustrated in Fig. 1 and all combinations of transmitter and receiver data $v_{ij}(t)$, the transmitted signal by element i and received by element j, the image at point (x, z) is described by (Holmes *et al.*, 2005)

ISSN 2176-5480

$$I_{\mathrm{TFM}}(x,z) = \sum_{i=1}^{N}\sum_{j=1}^{N} v_{ij}(\tau_{ij}(x,z)), \tag{1}$$

where $\tau_{ij}(x,z)$ is the time of flight between the transmitter i, the point (x,z) and the receiver j. This technique is also known as TFM (Total Focusing Method) and once only the amplitude data (in time domain) is used, the amplitude image is also called in this work as TFM image.

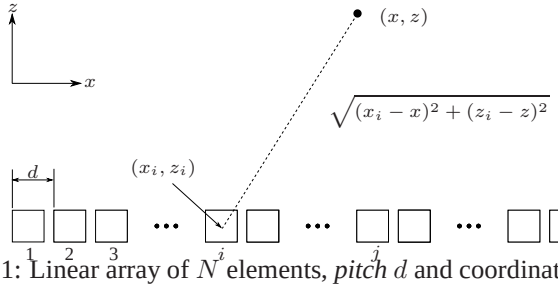

Figure 1: Linear array of N elements, *pitch* d and coordinate system.

When the pitch is greater than half-wavelength ($d > \lambda/2$) the array is called sparse (Lockwood *et al.*, 1996). The use of sparse arrays is interesting because it reduces the cost of the arrays as the processing and storage of signals, due to the reduction in data volume. For example, in order to obtain a TFM image using an N elements array, N^2 signals are processed for each point in the image, as indicated by Eq. (1). If the number of elements is reduced by two, there is a reduction in the number of signals by four, which accelerates the process of signal acquisition and processing. On the other hand they present grating lobes in the radiation pattern. These grating lobes have the same amplitude as the main lobe (for point sources) and they are related to artifacts, reducing image quality. An alternative is to break the periodic nature of the elements distribution by randomly removing elements, which reduces the grating lobes levels, but the average side lobe levels increases with the number of removed elements (Turnbull and Foster, 1991; Gavrilov *et al.*, 1997). Figure 2 presents the radiation pattern of three linear arrays: (i) with 16 elements and $\lambda/2$ pitch, (ii) with 8 elements and pitch of λ and (iii) with 8 elements randomly distributed with higher concentration of elements in the center of the array. These arrays configurations are indicated in Fig. 3.

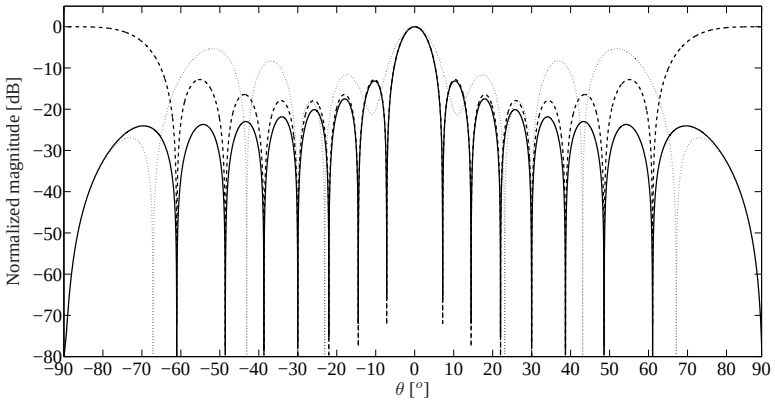

Figure 2: Radiation pattern of three linear arrays: one with 16 elements and $\lambda/2$ pitch (solid line), one with 8 elements and pitch of λ (dashed line) and another randomly distributed (dotted line).

The main lobe width, related to the lateral resolution, is the same for arrays (i) and (ii) because of the aperture size is also the same, but the grating lobes, shown in $\pm 90^o$, are presented only for the array (ii), with λ pitch. As expected, by breaking the periodicity of the elements distribution in array (iii), the grating lobes levels are reduced, but side lobes levels are increased.

Figure 4 presents the Point Spread Function (PSF) for a point reflector in $x = 0$ cm and $z = 25$ cm, considering the arrays of Fig. 3 and the TFM procedure described in Eq. (1). The PSF represents how a point reflector at a certain position is visualized by the array with the imaging technique. The waveform signals are simulated in Matlab with a four-cycles Gaussian envelope RF signal and central frequency of 330 kHz, propagating in an aluminum plate (wave speed of 5242 m/s). A random noise with Gaussian distribution and 10% of the signals magnitude is added to the synthesized signals.

ISSN 2176-5480

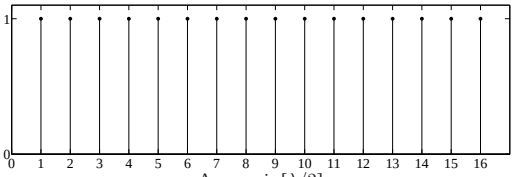

(a) Array (i).

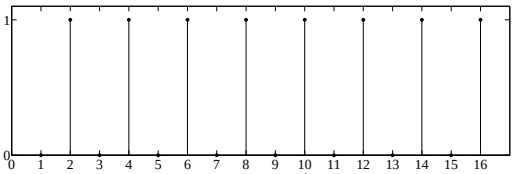

(b) Array (ii).

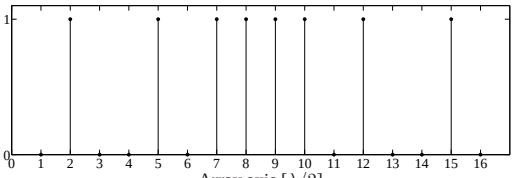

(c) Array (iii).

Figure 3: Arrays configuration simulated to obtain the radiation patterns of Fig. 2: (a) 16 elements array and pitch of $\lambda/2$, (b) 8 elements array and pitch of λ and (c) 8 elements array randomly distributed with higher concentration of elements in the center.

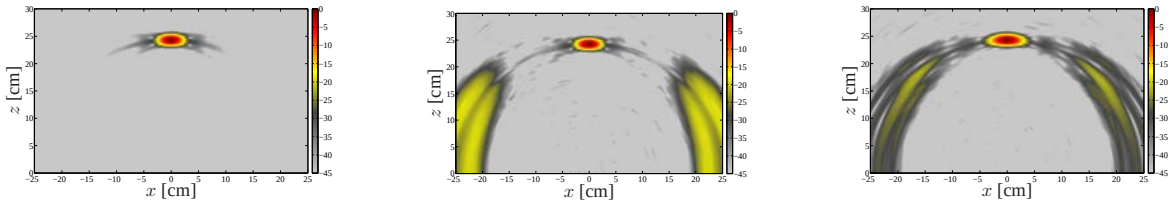

(a) Array (i). (b) Array (ii). (c) Array (iii).

Figure 4: PSF with TFM technique for a point reflector at 25 cm of the array and array configurations of Fig. 3: (a) array (i) - 16 elements array and pitch of $\lambda/2$, (b) array (ii) - 8 elements array and pitch of λ and (c) array (iii) - 8 elements array randomly distributed. Scales in dB.

Close to the point, the images are very similar for arrays (i) and (ii), due to the same main lobe width and side lobe levels (close to 0^o). The grating lobes results in image artifacts as the semicircle of radious between 20 cm and 25 cm and some shadows in all image around of Fig. 4b. The wider main lobe of array (iii) results in a larger point representation than the others. The image artifacts close to the point are stronger due to the increase of side lobes level, but far from the reflector the artifacts are reduced compared to the array (ii), as can be observed in the semicircle. According to Prado *et al.* (2013c), that tested similar sparse arrays configurations with an image compounding technique, the choice of the best sparse array configuration is not trivial, because it depends on the relative localization of the defects respect to the arrays and the radiation pattern of each configuration. In the work, by comparing the sparse arrays configurations, the periodic configuration presents better resolution and the randomly distributtion presents defects with higher intensities.

Even for full-populated array the use of SA imaging technique with TFM has important limitations because low signal-to-noise ratio and the penetration capability of the system is also low. Prado *et al.* (2012) and Higuti *et al.* (2010) show that the TFM images present: (a) large dead zone due to cross-talk, (b) limited resolution due to the wavelength, signal characteristics as period and number of cycles, main lobe width and side lobes levels and (c) artifacts due to multiple reflections between elements, defects and the edges of the plate, as well as grating lobes, in case of sparse arrays.

The study of the beamforming process based on the signals phase distribution has been shown a good practice to improve the quality of the images respect to these limitations. Camacho *et al.* (2009) present the analisys of the phase variance and Martínez-Graullera *et al.* (2011) the spectral analysis of the phase distribution. Both present coherence factors that are multiplied by the TFM images to improve contrast and dynamic range. The efficiency of coherence estimators based on phased distribution has been tested by Torbatian *et al.* (2010) for grating lobe suppression. Prado *et al.*

ISSN 2176-5480

(2012) reduced the dead zone by the procedure of multiplicate the TFM image by a phase image. Based on (Camacho *et al.*, 2009; Martínez-Graullera *et al.*, 2011), Prado *et al.* (2013a) use the instantaneous phase for improving the efects of grating lobes in SA images using only the pulse-echo signals of the aperture. The coherence factors, obtained by the phase information, have been resulted in high degree of robustness to noise, side and grating lobes efects, and can be also used as a indicator of the presence or not of a defect (Higuti *et al.*, 2010; Prado *et al.*, 2012, 2013c).

Three techniques using the phase information are compared to the conventional amplitude beamformer: the SCF - Sign Coherence Factor (Camacho *et al.*, 2009), which uses the phase diversity at the aperture data; the CFM - Coherence Factor Map (Martínez-Graullera *et al.*, 2011), that presents a spectral analysis of the phase dispersion; and the analysis of the instantaneous phase (Prado *et al.*, 2013b) image, which applies a threshold based on a statistical analysis of noise and the number of elements. The techniques are applied to full-populated and sparse arrays in non-destructive testing using Lamb waves to obtain images of an aluminum plate with artificial defects. The use of phase information results in dead zone reduction and contrast improvement. The SCF images have better resolution, contrast and less image artifacts than CFM images, which in turn presents defects with higher intensities. IP images have better contrast due to the threshold, and once it uses only the phase information, the attenuation effect due to propagation losses is less significant.

2. PHASE IMAGING METHODS

2.1 Sign Coherence Factor (SCF)

The SCF image is a method based on an analysis of the phase diversity at the aperture data. It can be computed as (Camacho *et al.*, 2009)

$$I_{\mathrm{SCF}}(x,z) = 1 - \sqrt{1 - \left[\frac{1}{N^2}\sum_{i=1}^{N}\sum_{j=1}^{N} b_{ij}(\tau_{ij}(x,z))\right]^2}, \tag{2}$$

where $b_{ij}(t)$ is the sign bit of the aperture data:

$$b_{ij}(t) = \begin{cases} -1, & \text{if} \quad v_{ij}(t) < 0 \\ 1, & \text{if} \quad v_{ij}(t) \geq 0 \end{cases}. \tag{3}$$

Once the variance σ^2 is easily computed from the average value of the signs of the aperture data as

$$\sigma^2 = 1 - \left[\frac{1}{N^2}\sum_{i=1}^{N}\sum_{j=1}^{N} b_{ij}(\tau_{ij}(x,z))\right]^2, \tag{4}$$

the Eq. (2) can be writen in the form:

$$I_{\mathrm{SCF}}(x,z) = 1 - \sigma, \tag{5}$$

where σ is the standard deviation of the polarity $b_{ij}(t)$ of the aperture data. The SCF measures the coincidence in algebraic sign of the received signals. Signals are defined as fully coherent if all of them have the same polarity ($I_{\mathrm{SCF}}(x,z) = 1$). In other cases the value of $I_{\mathrm{SCF}}(x,z)$ is in the range [0, 1[.

2.2 Coherence Factor Map (CFM)

The main inconvenience of the SCF method resides in the variance/standard deviation calculation, which limits its application in real time. Under this perspective, Martínez-Graullera *et al.* (2011) developed a new phase coherence descriptor, based on a spectral analysis and which resulted in a very straightforward and computational simple implementation method. The CFM is an alternative to the variance calculation and can be easily integrated to the TFM algorithm at a very low computational cost. The CFM contains a measurement of signal phase distribution combined at each pixel.

At each image point a set of signal phases is obtained that is sorted to compose a phase distribution function by a sum of Kronecker deltas:

$$P(\phi,x,z) = \sum_{i=1}^{N}\sum_{j=1}^{N} \delta\left[\phi - \phi_{ij}(\tau_{ij}(x,z))\right], \tag{6}$$

ISSN 2176-5480

where $\phi_{ij}(t)$ is the phase of the signal emitted by element i and collected by element j compensated at (x, z). These values are distributed in the $[-\pi, \pi[$ interval and can be extended to form the periodic signal using a function based on Dirac deltas:

$$\Phi(\phi, x, z) = \sum_{k=-\infty}^{\infty} \delta(\phi - k2\pi) * P(\phi, x, z). \tag{7}$$

The periodic extension of $P(\phi, x, z)$ is susceptible of being decomposed by Fourier Series into a sum of simple oscillating functions where each coefficient can be computed as

$$c_n(x, z) = \frac{1}{2\pi} \int_{-\pi}^{\pi} \Phi(\phi) e^{-jn\phi} \mathrm{d}\phi = \frac{1}{2\pi} \sum_{i=1}^{N} \sum_{j=1}^{N} e^{-jn\phi_{ij}(\tau_{ij}(x,z))}. \tag{8}$$

The signal $P(\phi, x, z)$ composed by a random distribution of phase spreads its energy over all the Fourier Coefficients which are low valued. However, when there is a concentration of phases it increases the presence of the sinusoidal components of period $1/2\pi$ than can be evaluated easily if $n = 1$ in Eq. (8). In order to normalize the result and obtain a more easy interpretation, the coherence factor at point (x, z) is defined as

$$I_{\mathrm{CFM}}(x, z) = 2\pi |c_1(x, z)| = \left| \sum_{i=1}^{N} \sum_{j=1}^{N} e^{-j\phi_{ij}(\tau_{ij}(x,z))} \right| = \left| \sum_{i=1}^{N} \sum_{j=1}^{N} \cos(\phi_{ij}(\tau_{ij}(x, z))) - j \sin(\phi_{ij}(\tau_{ij}(x, z))) \right|. \tag{9}$$

The set of complete signals $v_{ij}(t)$, for $i, j = 1, 2 \cdots N$, can be expressed be presented as modulus and phase components:

$$v_{ij}(t) = V_{ij}(t) e^{\phi_{ij}(t)} = V_{ij} \cos(\phi_{ij}(t)) + jV_{ij} \sin(\phi_{ij}(t)), \tag{10}$$

where $V_{ij}(t)$ and $\phi_{ij}(t)$ is obtained by calculating the modulus and phase of the analytic signal $v_{aij}(t)$, respectively. The analytic signal of $v_{ij}(t)$ is given by (Oppenheim *et al.*, 1999)

$$v_{aij}(t) = v_{ij}(t) + j\hat{v}_{ij}(t), \tag{11}$$

where $\hat{v}_{ij}(t)$ is the Hilbert transform of $v_{ij}(t)$.

Then the Eq. (9) can be computed from the in-phase and quadrature signals as

$$I_{\mathrm{CFM}}(x, z) = \frac{1}{N^2} \left[\left(\sum_{i=1}^{N} \sum_{j=1}^{N} \frac{v_{ij}(\tau_{ij}(x, z))}{V_{ij}(\tau_{ij}(x, z))} \right)^2 + \left(\sum_{i=1}^{N} \sum_{j=1}^{N} \frac{\hat{v}_{ij}(\tau_{ij}(x, z))}{V_{ij}(\tau_{ij}(x, z))} \right)^2 \right]^{1/2}. \tag{12}$$

The value of $I_{\mathrm{CFM}}(x, z)$ is also in the range [0, 1] and is directly proportional to the number of signals that collaborates coherently to compose the pixel: if $I_{\mathrm{CFM}}(x, z) = 0.5$, then 50% of the signals match in phase and if $I_{\mathrm{CFM}}(x, z) = 1.0$, the defect is detected by all signal combinations.

2.3 Instantaneous Phase (IP) Image

The IP image is defined by using the instantaneous phase $\phi_{ij}(t)$ instead of the amplitude signal in the Eq. (1) (Prado *et al.*, 2013b):

$$I_{\mathrm{IP}}(x, z) = \frac{1}{N^2} \sum_{i=1}^{N} \sum_{j=1}^{N} \phi_{ij}(\tau_{ij}(x, z)). \tag{13}$$

To be considered a reflector the $I_{\mathrm{IP}}(x, z)$ must be above a threshold ϵ, which depends on the standard deviation of the average $\bar{\sigma_0}$, written as

ISSN 2176-5480

$$\epsilon = \sqrt{\bar{\sigma_0}}, \tag{14}$$

where

$$\bar{\sigma_0} = \frac{\sigma_0}{\sqrt{N_s}}, \tag{15}$$

which in turn depends on the standard deviation of the noise phase distribution σ_0 and the number of signals used to obtain the image N_s, that is equal to N^2 in the cases described in Eq. (1) and Eq. (13).

For a point (x, z), which there is not a reflector, the IP is related to a random noise, which is uniformly distributed over 2π and then $\sigma_0 = \pi/\sqrt{3}$ (Carlson and Crilly, 2009). In this case the IP image is multiplied by the standard deviation of the average and the final image is:

$$I_{\text{IP}_{\text{final}}}(x,z) = I_{\text{IP}}(x,z) \times \begin{cases} 1, & \text{if} \quad |I_{\text{IP}}(x,z)| \geq \epsilon \\ \bar{\sigma_0}, & \text{if} \quad |I_{\text{IP}}(x,z)| < \epsilon \end{cases} . \tag{16}$$

3. EXPERIMENTAL SETUP

A linear array consisting of 16 piezoelectric elements (Ferroperm PZ26, 7 mm $\times$ 6 mm $\times$ 0.5 mm) with 9 mm pitch ($\sim \lambda/2$) is mounted at the border of a 1 mm thickness isotropic aluminum plate (1 m $\times$ 1.24 m) with artificial defects, illustrated in Fig. 5.

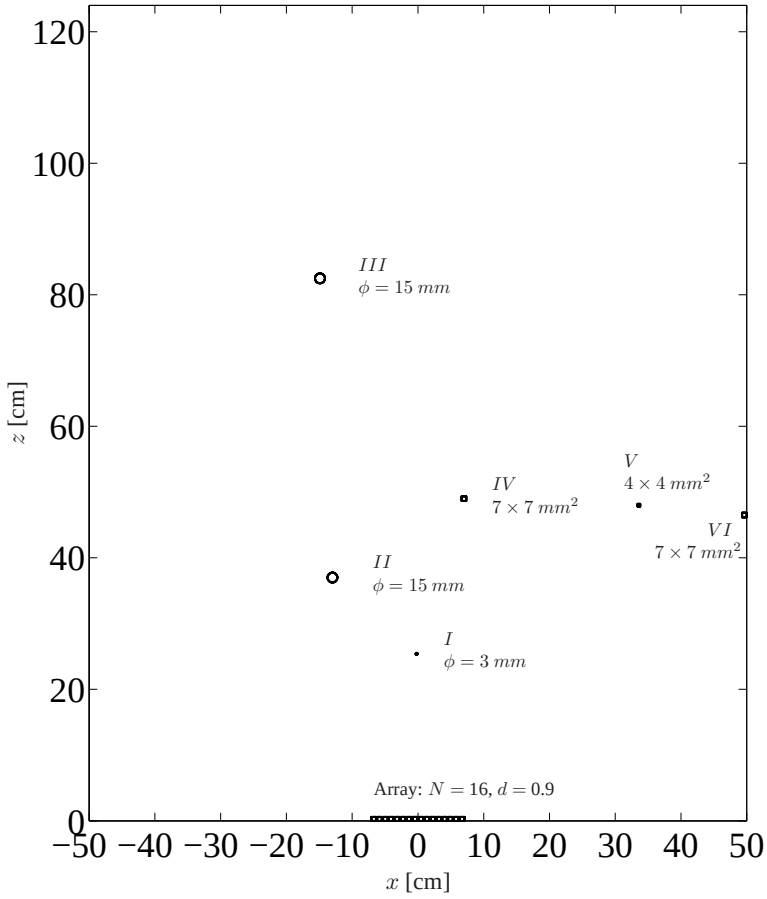

Figure 5: Aluminum plate with defects. The center of the array is at $(x,\ z) = (0,\ 0)$.

The central coordinates (x, z) of the defects with their dimensions (diameter ϕ for circular and area for square defects), geometries and types are presented in Tab. 1. There is a through hole (defect I) and the surface defects are thin piezoceramics ($\sim$ 0.5 mm thickness) attached to the plate. The addition of a mass to a point on the plate changes the acoustic

ISSN 2176-5480

impedance at that point, causing reflections of the incident wave, in a similar way to that of a defect, without damaging the plate (Konstantinidis *et al.*, 2006). All defects dimensions are smaller than the wavelength (15.9 mm), which reduces the quality of the image regarding to the size of the defects.

Table 1: Artificial defects produced in the aluminum plate.

Defect	x [cm]	z [cm]	Dimension	Geometry	Type
I	-0.2	25.4	3.0 mm	circular	hole
II	-13.0	37.0	15.0 mm	circular	surface
III	-14.9	82.5	15.0 mm	circular	surface
IV	7.0	49.0	49.0 mm^2	square	surface
V	33	48.0	16.0 mm^2	square	surface
VI	49.6	46.5	49.0 mm^2	square	surface

The piezoceramics are excited by a waveform generator (Tektronix AFG3101, 14 bits resolution) with a 120 V peak-to-peak 4 cycles Gaussian envelope RF signal at 330 kHz, coupling the fundamental symmetric mode S0 with low dispersion and wave speed of 5242 m/s. The data acquisition is done using a digital oscilloscope (Agilent MSO7014B, 10 bits resolution in average mode), using 16 averages. A 32 channels multiplexer is used to obtain all the transmit-receive combinations used in the beamforming techniques.

4. RESULTS AND DISCUSSIONS

The TFM image of the plate is illustrated in Fig. 6. Defects I, II, III, IV and V are detected (only defect VI is not detected), but a several image artifacts in all image around, mainly close to the array are also presented, which could be interpreted as defects or make defects being considered as artifacts. A region of the plate was defined for imaging: -50 $< x <$ 50, 0 $< z <$ 100 [cm] with 1 mm of resolution in both directions. The plate end at $z = 124$ cm was not shown because there was no defect close to it.

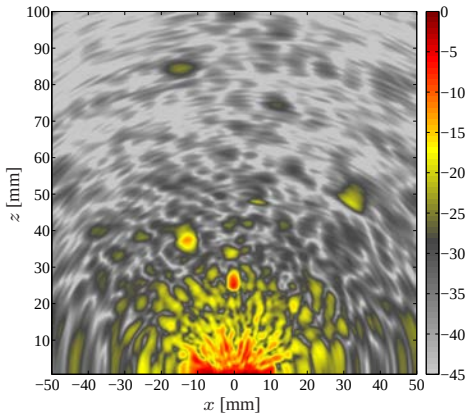

Figure 6: TFM image of the plate. Scale in dB.

The high intensity region close to the array is called dead zone. It is caused by the mechanical coupling between the elements of the array. The time of flight of the direct propagation and multiple reflections between the elements is short when compared to the echoes coming from defects. Therefore it reduces defects contrasts.

Figure 7 presents the phase images (SCF, CFM and IP). The SCF image represents defects with better resolution, less artifacts and background noise than the others. On the other hand, in CFM and IP images the defects have higher intensities, for example for defect VI, which is not considered in TFM image, and defects III and IV (see also Fig. 5 as a reference). Comparing the CFM to IP images, the first presents defects with higher intensities and in the second the image artifacts are presented with lower intensities.

As expected, from the phase images characteristics observed in Fig. 7, the multiplication of them by the TFM image, illustrated in Fig. 8, results in dead zone reduction compared to the amplitude image. Besides, the multiplication by the SCF image results in better resolution and less image artifacts. On the other hand the CFM image produces defects representation with higher intesities than SCF. The background for the IP final image is higher than others due to the use of IP image instead of TFM, which reduces the contrast, as observed in Fig. 7c. Once it uses only the phase information, the attenuation effect due to propagation losses is less significant, as can be observed in higher intensity for defect III,

ISSN 2176-5480

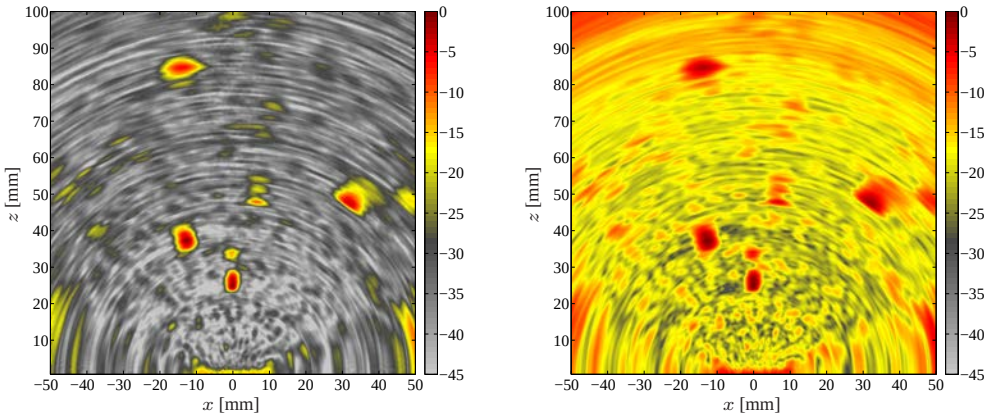

(a) $I_{\text{SCF}}(x, z)$.

(b) $I_{\text{CFM}}(x, z)$.

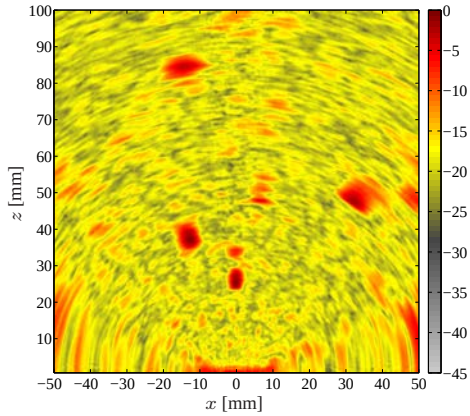

(c) $I_{\text{IP}}(x, z)$.

Figure 7: Phase images of the plate: (a) SCF, (b) CFM and (c) IP. Scales in dB.

the farther from array. Other important observation is that defect VI is only significantly detected by this method. In all images the lateral plate ends reflections as well as the elements of the array can be observed.

A threshold could be applied to the SCF and CFM methods, improving their contrasts as well to use these techniques to indicate the presence or not of a defect, but a well determined value should be determined. The IP threshold (ϵ) is based on the the standard deviation of the phase in the absence of a reflector and the number of array elements. A threshold based on a percentage of the maximum value in the image could be used, but higher values are related to low sensitivity and some defects would not be considered, as well as low values should increase the artifacts intensities, as observed by Prado *et al.* (2013c) and Higuti *et al.* (2010).

Table 2 presents the defects contrasts considering a line at the center of the defects, parallel to the array and Fig. 9 illustrates a line in $z = 48.1$ cm, close to defects IV, V and VI, either parallel to the array. SCF image produces defects representation with better resolution and contrast. The contrast for CFM and IP methods are similar, but resolution is better for CFM and defect VI is better represented by IP, even when compared to the SCF.

Table 2: Defects contrasts for each technique. Values in dB.

Technique ↓, Defect →	I	II	III	IV	V	VI
$I_{\text{TFM}}(x, z)$	21.3	22.1	15.2	13.8	15.5	4.4
$I_{\text{TFM}}(x, z) \times I_{\text{SCF}}(x, z)$	55.7	57.3	44.0	37.6	44.5	13.6
$I_{\text{TFM}}(x, z) \times I_{\text{CFM}}(x, z)$	38.3	40.4	24.1	26.4	30.9	9.1
$I_{\text{IP}_{\text{final}}}(x, z)$	34.1	35.0	32.5	26.8	33.6	22.1

From the same dataset some signals are discarded for imaging the plate with the sparse arrays configurations of Fig. 3b and Fig. 3c. The obtained images are illustrated in Fig. 10 and Fig. 11. As observed in Fig. 2, the array (ii) has significant grating lobes, which explains the several image artifacts in images of Fig. 10. For the array configuration (iii) the grating

ISSN 2176-5480

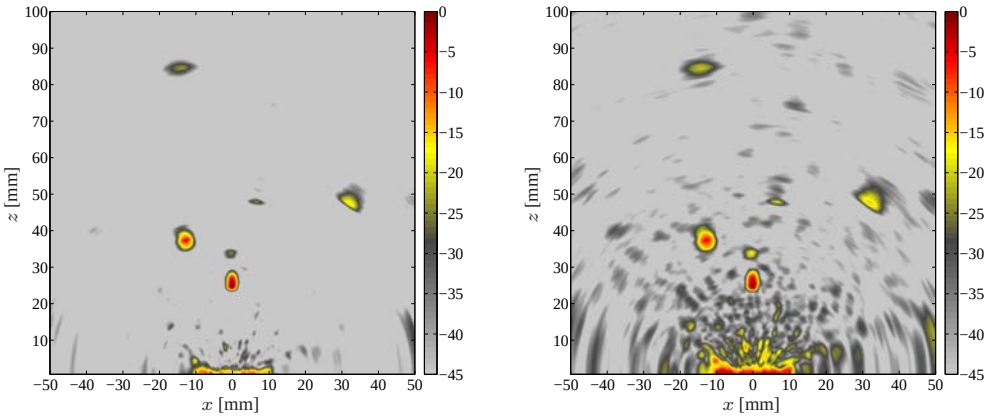

(a) $I_{\mathrm{TFM}}(x,z) \times I_{\mathrm{SCF}}(x,z)$.

(b) $I_{\mathrm{TFM}}(x,z) \times I_{\mathrm{CFM}}(x,z)$.

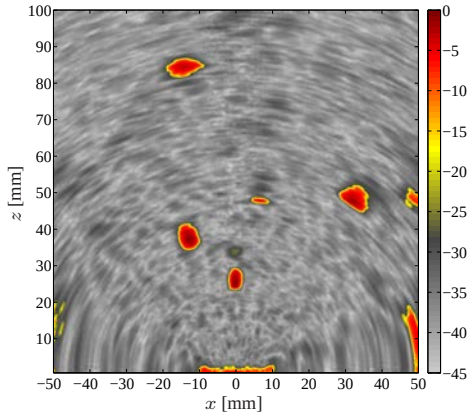

(c) $I_{\mathrm{IP}_{\mathrm{final}}}(x,z)$.

Figure 8: TFM images multiplied by: (a) SCF and (b) CFM images and (c) final image obtained by the IP. Scales in dB.

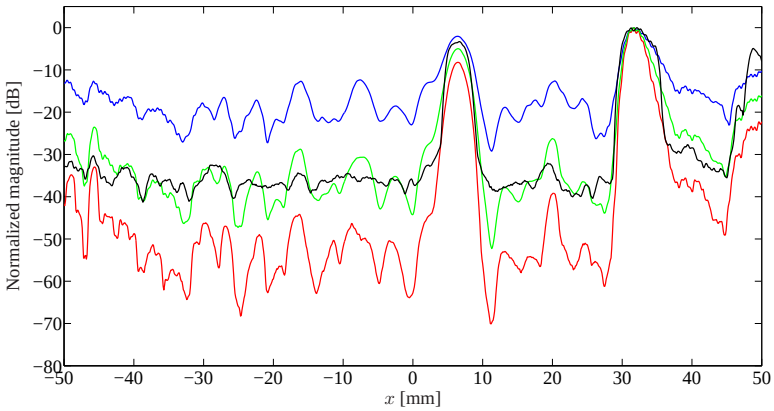

Figure 9: Lateral view in $z = 48.1$ cm close to defects IV, V and VI: TFM image (blue), it multiplied by SCF (red) and CFM (green) images and final image obtained by the IP (black) .

lobes are reduced, but side lobes levels between 30^o and 60^o are increased, that could be the cause of less sensitivity to defects in these directions.

For both cases there are few elements in the array, which reduces significantly the signal-to-noise ratio, and consequently the quality of images. Even so the phase techniques results in significant improvements respect to dead zone, contrast and image artifacts when compared to TFM method. Similar to full-populated array results are obtained by comparing the SCF to CFM images respect to resolution and artifacts, but defects intensities are higher for SCF images. The IP technique uses a threshold based on a statistical analysis of the phase noise to consider the signal acquired as defect or

ISSN 2176-5480

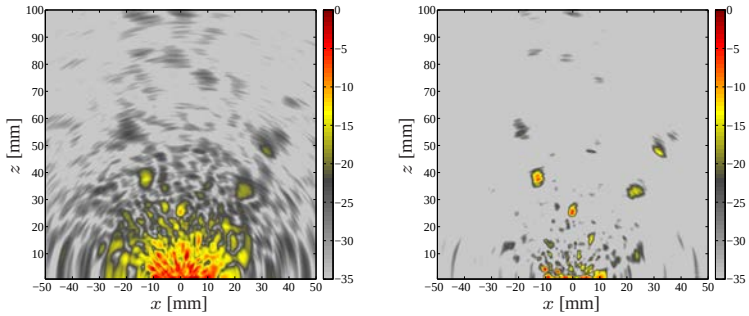

(a) $I_{\text{TFM}}(x,z)$. (b) $I_{\text{TFM}}(x,z) \times I_{\text{SCF}}(x,z)$.

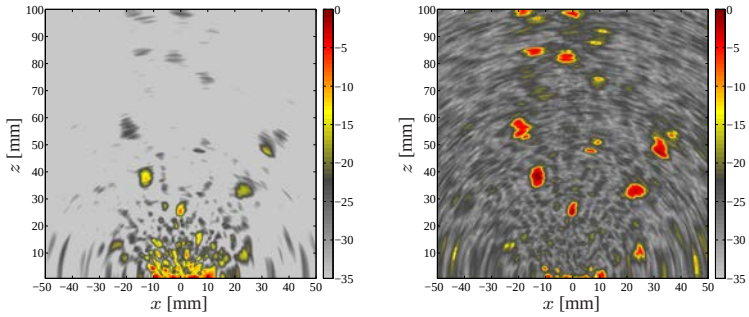

(c) $I_{\text{TFM}}(x,z) \times I_{\text{CFM}}(x,z)$. (d) $I_{\text{IP}_{\text{final}}}(x,z)$.

Figure 10: Images obtained for the sparse array of Fig. 3b: (a) TFM image and TFM image multiplied by (b) SCF and (c) CFM images, and (d) final image obtained by the IP. Scales in dB.

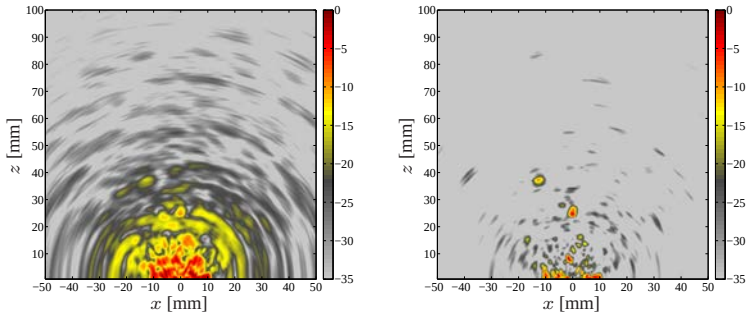

(a) $I_{\text{TFM}}(x,z)$. (b) $I_{\text{TFM}}(x,z) \times I_{\text{SCF}}(x,z)$.

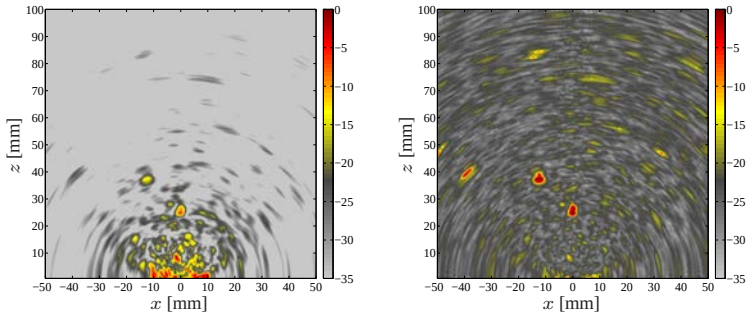

(c) $I_{\text{TFM}}(x,z) \times I_{\text{CFM}}(x,z)$. (d) $I_{\text{IP}_{\text{final}}}(x,z)$.

Figure 11: Images obtained for the sparse array of Fig. 3c: ((a) TFM image and TFM image multiplied by (b) SCF and (c) CFM images, and (d) final image obtained by the IP. Scales in dB.

noise. This consideration is truer for the higher is the number of signals used for imaging, which explain the bad results obtained with this procedure. Nevertheless defect III (the farther from array) is better represented by the $I_{\text{IP}_{\text{final}}}(x,z)$ as

ISSN 2176-5480

well as dead zone reduction.

5. CONCLUSIONS

Three techniques using the phase information are compared to the conventional amplitude descriptor for full-populated and sparse arrays in non-destructive testing of a plate-like structure using Lamb waves. The use of phase information is better than only the amplitude for all cases, reducing dead zone and improving contrast. For full-populated array, the SCF images have better resolution, contrast and image artifacts than CFM images, which in turn present defects with higher intensities. IP and CFM images results in similar contrasts to each other and the IP method obtains better defect representations for farther defects, once uses only the phase information and the attenuation effect due to propagation losses is less significant. For the same reason, the background intensity is high, which reduces the contrast. Even so, defect VI, close to the lateral border, is represented only in the final image obtained from the IP information.

The results for sparse arrays are affected by the small number of elements, that reduces the signal-to-noise ratio. Even so the phase techniques results in significant improvements respect to dead zone, contrast and image artifacts when compared to TFM method. Similar to full-populated array results are obtained by comparing the SCF to CFM images respect to resolution and artifacts, but defects intensities are higher for SCF images. The IP technique has been show limited when the number of signals used for imaging is small, due to the statistical analysis of the phase signals of the aperture. Anyway defect III is better represented by this method.

Phase images can also be used as indicator for the presence or absence of a defect in the analyzed pixel. The use of a percentage of maximum value in SCF and CFM images could be considered, but high values are related to low sensitivity and some defects would not be considered, as well as low values should increase the artifacts intensities. In this case, the higher intensities of defects representation of CFM images could be better compared to SCF images. The IP method presents a well determined threshold value, based on the standard deviation of the phase in the absence of a reflector and the number of array elements, detecting all defects for the full-populated array.

6. ACKNOWLEDGEMENTS

The authors would like to thank the financial support from FAPESP (2010/02240-0, 2010/16400-0, 2013/00330-0), Capes and CNPq (560825/2010-2) in Brazil.

7. REFERENCES

Alleyne, D.N. and Cawley, P., 1992. "Optimization of Lamb wave inspection techniques". *NDT&E International*, Vol. 25, No. 1, pp. 11 – 22.

Camacho, J., Parrilla, M. and Fritsch, C., 2009. "Phase coherence imaging". *IEEE Transactions on Ultrasonics, Ferroelectrics, and Frequency Control*, Vol. 56, No. 5, pp. 958 –974.

Carlson, A.B. and Crilly, P.B., 2009. *Communication Systems*. McGraw-Hill Higher Education.

Diamanti, K., Soutis, C. and Hodgkinson, J., 2007. "Piezoelectric transducer arrangement for the inspection of large composite structures". *Composites Part A: Applied Science and Manufacturing*, Vol. 38, No. 4, pp. 1121 – 1130.

Drinkwater, B.W. and Wilcox, P.D., 2006. "Ultrasonic arrays for non-destructive evaluation: A review". *NDT&E International*, Vol. 39, No. 7, pp. 525 – 541.

Gavrilov, L., Hand, J.W., Abel, P. and Cain, C.A., 1997. "A method of reducing grating lobes associated with an ultrasound linear phased array intended for transrectal thermotherapy". *Ultrasonics, Ferroelectrics and Frequency Control, IEEE Transactions on*, Vol. 44, No. 5, pp. 1010 –1017.

Higuti, R.T., Martínez-Graullera, O., Martín, C.J., Octavio, A., Elvira, L. and Montero de Espinosa, F., 2010. "Damage characterization using guided-wave linear arrays and image compounding techniques". *IEEE Transactions on Ultrasonics, Ferroelectrics, and Frequency Control*, Vol. 57, No. 9, pp. 1985 –1995.

Holmes, C., Drinkwater, B.W. and Wilcox, P.D., 2005. "Post-processing of the full matrix of ultrasonic transmit-receive array data for non-destructive evaluation". *NDT&E International*, Vol. 38, No. 8, pp. 701 – 711.

Konstantinidis, G., Drinkwater, B.W. and Wilcox, P.D., 2006. "The temperature stability of guided wave structural health monitoring systems". *Smart Mater. Struct.*, Vol. 15, pp. 967–976.

Lockwood, G., Li, P.C., O'Donnell, M. and Foster, F., 1996. "Optimizing the radiation pattern of sparse periodic linear arrays". *Ultrasonics, Ferroelectrics and Frequency Control, IEEE Transactions on*, Vol. 43, No. 1, pp. 7 –14.

Martínez-Graullera, O., Romero-Laorden, D., Martín-Arguedas, C.J., Ibañez, A. and Ullate, L.G., 2011. "A new beamforming process based on the phase dispersion analysis". In *Proceedings of the International Congress on Ultrasonics*. Vol. 1433, pp. 185–188.

Michaels, J.E., 2008. "Detection, localization and characterization of damage in plates with an *in situ* array of spatially distributed ultrasonic sensors". *Smart Materials and Structures*, Vol. 17, No. 3, pp. 1 – 15.

Oppenheim, A.V., Schafer, R.W. and Buck, J.R., 1999. *Discrete-Time Signal Processing*. Upper Saddle River, New Jersey.

ISSN 2176-5480

Prado, V.T., Higuti, R.T., Kitano, C. and Martínez-Graullera, O., 2013b. "The use of instantaneous phase for improving sparse arrays images". In *2013 IEEE International Ultrasonics Symposium (IUS)*.

Prado, V.T., Higuti, R.T., Kitano, C. and Martínez-Graullera, O., 2013c. "Sparse arrays and image compounding techniques for non-destructive testing using guided acoustic waves". *Journal of Control, Automation and Electrical Systems*, Vol. 24, No. 3, pp. 263–271.

Prado, V.T., Higuti, R.T., Kitano, C., Martínez-Graullera, O. and Adamowski, J.C., 2012. "Technique to combine images produced by different propagation modes of guided waves for damage detection and contrast improvement in plate-like structures". In *2012 IEEE International Ultrasonics Symposium (IUS)*.

Prado, V.T., Higuti, R.T., Kitano, C., Martínez-Graullera, O. and Granja, S.C.G., 2013a. "The use of instantaneous phase for improving SAFT images". In *Proceedings of the 2013 International Congress on Ultrasonics*. pp. 458–463.

Rose, J.L., 2000. "Guided wave nuances for ultrasonic nondestructive evaluation". *IEEE Transactions on Ultrasonics, Ferroelectrics, and Frequency Control*, Vol. 47, No. 3, pp. 575–583.

Su, Z., Ye, L. and Lu, Y., 2006. "Guided Lamb waves for identification of damage in composite structures: A review". *Journal of Sound and Vibration*, Vol. 295, pp. 753–780.

Torbatian, Z., Adamson, R., Bance, M. and Brown, J.A., 2010. "A split-aperture transmit beamforming technique with phase coherence grating lobe suppression". *IEEE Transactions on Ultrasonics, Ferroelectrics, and Frequency Control*, Vol. 57, No. 11, pp. 2588–2595.

Turnbull, D.H. and Foster, F.S., 1991. "Beam steering with pulsed two-dimensional transducer arrays". *Ultrasonics, Ferroelectrics and Frequency Control, IEEE Transactions on*, Vol. 38, No. 4, pp. 320 –333.

Ylitalo, J.T. and Ermert, H., 1994. "Ultrasound synthetic aperture imaging: monostatic approach". *Ultrasonics, Ferroelectrics and Frequency Control, IEEE Transactions on*, Vol. 41, No. 3, pp. 333 –339.

Yu, L. and Giurgiutiu, V., 2007. "Omnidirectional guided wave pwas phased array for thin-wall structure damage detection". In *SPIE Procedings - Health Monitoring and Structural and Biological Systems*. Vol. 6529, pp. 652939.1 – 652939.12.

8. RESPONSIBILITY NOTICE

The authors are the only responsible for the printed material included in this paper.